A Parametric Sizing Model for Molten Regolith Electrolysis Reactors to Produce Oxygen from Lunar Regolith

Samuel S. Schreiner[1,*]

Massachusetts Institute of Technology, 77 Massachusetts Avenue, Cambridge, MA 02139

Jesus A. Dominguez[2], Laurent Sibille[3]

NASA Kennedy Space Center, Florida 32899

Jeffrey A. Hoffman[4]

Massachusetts Institute of Technology, 77 Massachusetts Avenue, Cambridge, MA 02139

Abstract

We present a parametric sizing model for a Molten Electrolysis Reactor that produces oxygen and molten metals from lunar regolith. The model has a foundation of regolith material properties validated using data from Apollo samples and simulants. A multiphysics simulation of an MRE reactor is developed and leveraged to generate a vast database of reactor performance and design trends. A novel design methodology is created which utilizes this database to parametrically design an MRE reactor that 1) can sustain the required mass of molten regolith, current, and operating temperature to meet the desired oxygen production level, 2) can operate for long durations via joule heated, cold wall operation in which molten regolith does not touch the reactor side walls, 3) can support a range of electrode separations to enable operational flexibility. Mass, power, and performance estimates for

*Corresponding author

Email address: schr0910@umn.edu (Samuel S. Schreiner)

[1]NASA Space Technology Research Fellow, MIT Department of Aeronautics and Astronautics

[2]VENCORE-ESC, NASA Kennedy Space Center

[3]Surface Systems Group, ESC-5, NASA Kennedy Space Center

[4]Professor of the Practice, MIT Department of Aeronautics and Astronautics

an MRE reactor are presented for a range of oxygen production levels. The effects of several design variables are explored, including operating temperature, regolith type/composition, batch time, and the degree of operational flexibility.

Keywords: molten regolith, electrolysis, lunar regolith, In Situ Resource Utilization, ISRU, lunar oxygen production, moon

---

1. Introduction

1.1. ISRU Motivation

One of the most significant barriers to space exploration is the burden of bringing all of the material resources from Earth required for a mission. The rocket equation (Turner, 2008) describes how a small increase in payload mass results in a dramatic increase in the total mass of the required launch system. This paradigm has limited space exploration with launch costs on the order of $10,000/kg to low-earth orbit (LEO) (Rapp, 2007) and $110,000/kg to the lunar surface (Diaz et al., 2005), in 2015 dollars . To enable sustainable, affordable exploration of the solar system, the reliance on Earth's resources must be reduced.

In-situ resource utilization (ISRU) is *"the collection, processing, storing and use of materials encountered in the course of human or robotic space exploration that replace materials that would otherwise be brought from Earth"* (Sacksteder and Sanders, 2007). One form of ISRU is producing oxygen from lunar regolith. Oxygen is a major component of launch vehicle, spacecraft, and lander masses – 80% of launch vehicle mass is fuel and oxygen (Badescu, 2012), which translates to around 70% oxygen by weight. At the same time, oxygen is one of the most abundant lunar resources – lunar soil is around 44% oxygen by weight (Badescu, 2012). The production of this valuable resource outside of Earth's gravity well can support lunar surface activities and enable orbital refueling to reduce the amount of resources that must be launched from Earth.

Although a number of analyses have examined the utility of lunar oxygen production (Simon, 1985; Joosten and Guerra, 1993; Duke et al., 2003), the accuracy of their findings often depend heavily on the mass and performance of the ISRU systems involved. Sherwood and Woodcock (1993) conducted an extensive economic analysis of lunar oxygen production and calculated a cost of $18,370/kg (2015 dollars) to produce oxygen on the lunar surface.

However, they noted that, *"the sensitivities* [of their economic model] *are modest, except for the mass of production hardware."* When the ISRU system mass was varied by a factor of two, the oxygen production cost varied from $12,570 to $29,857/kg in 2015 dollars. Simon (1985) also showed that, after the Earth-to-Moon transportation cost, the power required for ISRU had the biggest impact on the economic feasibility of lunar ISRU. To understand the appropriate applications of lunar ISRU, it is imperative to accurately model the mass, power and performance of ISRU systems.

1.2. Molten Regolith Electrolysis Process Overview

One promising oxygen production technique, called Molten Regolith Electrolysis (or Molten Oxide Electrolysis), has received little modeling attention to date, despite it's significant potential. In the MRE process, lunar regolith is fed into a reactor where it is heated to a molten state. Molten lunar regolith is conductive enough to sustain direct electrolysis (Lindstrom and Haskin, 1979), in which a voltage is applied across two electrodes immersed in the molten regolith to drive a current. Oxygen gas is produced at the anode and molten metals and metalloids, such as iron, silicon, aluminum, and titanium, are produced at the cathode (Jarrett et al., 1980).

1.3. Motivation for Modeling MRE Reactors

There is a strong impetus to explore the feasibility of an ISRU system with an MRE reactor, as there are many potential benefits to such a system. A study comparing oxygen production methods, including water extraction from lunar polar craters, identified MRE has having the most favorable power consumption and the second most favorable mass throughput (Mason, 1992).

MRE does not require additional process materials, such as hydrogen, methane, or fluxing reagents. This means that an MRE reactor will not require additional systems to recycle the reagents, leading to a decrease in system mass and complexity. Depending on process conditions, MRE can extract up to 95% of the oxygen from lunar regolith, which dramatically decreases regolith throughput requirements and reactor mass and power.

With post-reactor processing, the byproducts of MRE (molten iron, silicon, aluminum, titanium, and glassy slag) can be used to produce infrastructure, spare parts and even solar arrays on the lunar surface (Landis, 2005; Curreri et al., 2006; Badescu, 2012). In fact, MRE is also being developed for environmentally-friendly metal production on Earth with a zero-carbon footprint (Gmitter, 2008; Vai et al., 2010).

1.4. Historical Development of Molten Regolith Electrolysis

The process of electrolytically extracting metals from molten ores was first patented by Aiken (1906) for the production of iron from raw ore. Carr (1963) first suggested using an electrolysis process to produce oxygen from lunar soil and the earliest experimental work on electrolytically reducing lunar soil simulants was conducted by Kesterke (1970). These experimental runs produced 170g of oxygen and significant amounts of iron, titanium, aluminum, and magnesium using an iridium anode and silica-carbide cathode. In the ensuing decades, MRE underwent considerable laboratory development (Jarrett et al., 1980; Lindstrom and Haskin, 1979; Carroll, 1983; Haskin et al., 1992).

Under the Vision for Space Exploration, further MRE development continued at MIT (Wang et al., 2011), Kennedy Space Center (Sibille et al., 2009, 2010), The Ohio State University (Standish, 2010), and Marshall Space Flight Center (Curreri et al., 2006). Many suitable anode materials were demonstrated, including iridium, platinum, rhodium (Gmitter, 2008), iridium-plated graphite (Paramore, 2010), 50-50 iridium/tungsten alloys (Vai et al., 2010), and iron-chromium alloys (Allanore et al., 2013). Reactor designs were scaled up from 0.1 A with 0.3 cm^2 electrodes to 10 A with 10 cm^2 electrodes (Vai et al., 2010; Sirk et al., 2010), making progress from laboratory-scale testing towards technology demonstration levels.

1.5. Molten Regolith Containment: Joule Heated Cold Wall Operation

Perhaps the most challenging design consideration in an MRE reactor is the containment of corrosive molten regolith. The longest laboratory experiments lasted on the order of a few hours (Paramore, 2010) before the molten regolith eroded through the inner crucible. Paramore (2010) noted that *"fortunately, this frustration* [crucible failure] *is purely an artifact of laboratory-scale experimentation."*

To solve the challenge of molten material containment, an MRE reactor can be designed similarly to industrial Hall-Heroult reactors to support joule heated, cold wall (JHCW) operation (Carroll, 1983; Sibille and Dominguez, 2012). In JHCW operation, the the current traveling through the resistive molten regolith generates heat via joule heating (I^2R) to maintain a central molten core, and the thermal gradients are designed such that the molten core is insulated by solid "frozen" regolith around the perimeter of the reactor. The solid regolith in contact with the reactor walls is not corrosive

and enables long duration operation. The reactor shown in Figure 1 demonstrates JHCW operation, with the central molten core surrounded by a phase boundary where the transition to the solid/glass phase occurs. The current streamlines are depicted in red and simplified anodic and cathodic reactions are indicated.

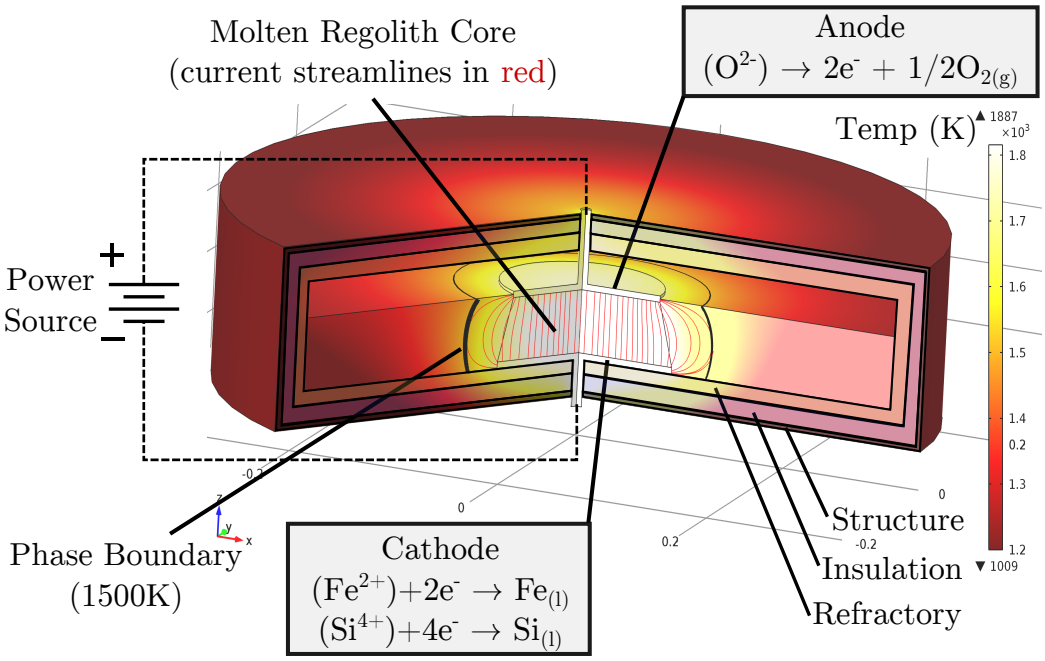

Figure 1: Schematic of a Molten Regolith Electrolysis Reactor that produces oxygen gas at the anode and molten metals at the cathode. The central molten core is insulated by solid "frozen" regolith around the reactor perimeter.

1.6. The Need for MRE Reactor Modeling

There is a large impetus to model MRE reactors. Altenberg (1990) noted that two of the primary issues associated with MRE were **1)** the lack of specified optimal process, conditions, feed rate, and feedstock requirements and **2)** a poor understanding of the meaningful design parameters and oxygen extraction efficiency. Colson and Haskin (1990) hypothesized that *"high melt resistivities coupled with the large distance between electrodes that would seem to be required to make the approach robust might make power requirements prohibitive* [for an MRE reactor]". Teeple (1994) surmised that *"the electrolysis techniques* [including MRE], *involve high temperatures, so one*

would expect high plant masses". This uncertainty concerning the operating conditions and expected mass and power of an MRE reactor can be reduced through extensive modeling of MRE reactors.

Although parametric models to predict the mass and power of reactors utilizing other oxygen extraction process have been developed (Hegde et al., 2009; Balasubramaniam et al., 2010), a similar model of suitable fidelity for an MRE reactor does not yet exist in the literature. This deficit has prevented quantitative comparisons between MRE and other processing techniques (Chepko, 2009).

Furthermore, MRE modeling can guide hardware development. During the experiments at MIT, the design of a JHCW reactor was avoided because *"at this stage* [fabricating a JHCW reactor] *was considered a superfluous enterprise, because the cell dimensions necessary to achieve sufficient joule heating would be extremely expensive to construct for an unproven process"*. Clearly, a better understanding of how to design JHCW reactors is needed in order to guide hardware development.

Previous MRE reactor simulations (Dominguez et al., 2009; Sibille and Dominguez, 2012) demonstrated that a JHCW MRE reactor appears feasible, but they developed a point design rather than a parametric model. That is, the simulation did not parametrically design a reactor, with mass and power estimates, to meet a given oxygen production level. With the advent of new regolith material property models in the high temperature regime (Schreiner et al., 2016), the time for an updated MRE reactor model is ripe. Furthermore, the most recent simulations and experimental work have studied reactors that use tens of amps of current, while production-level reactors will need to use on the order of kilo-amps. The proper method for scaling up MRE reactor designs to these higher production levels can be explored using MRE reactor modeling.

1.7. MRE Reactor Model Overview

To this end, we develop a sizing model for an MRE reactor that parametrically generates reactor design and performance estimates for a given set of inputs, including oxygen production level, operating temperature, and regolith feedstock type. This model can be used to **1)** guide MRE reactor design development, **2)** quantitatively compare MRE to other oxygen production techniques, and **3)** better understand how MRE reactors scale with production level.

The MRE reactor model has a foundation of lunar regolith material property models, described in Schreiner et al. (2016), which are validated using data from Apollo samples and regolith simulants. The reactor model calculates the regolith throughput (Section 2) and electrochemical voltage and current (Section 3) required to meet the desired oxygen production level.

The regolith material property models are integrated into a multiphysics simulation, described in Section 4, that simulates the electrical, chemical, and thermodynamic behavior of MRE reactor designs. The simulation is leveraged to create an extensive tradespace of reactor designs with different values for the diameter, electrode separation, and wall thermal conductivity.

As detailed in Section 5, the reactor model parametrically generates a reactor design (diameter, electrode separation, and wall thermal properties) that **1)** sustains the amount of molten mass and average current required to meet a given oxygen production level, **2)** maintains a given operating temperature within the molten core, and **3)** ensures that the reactor walls are insulated from the molten core by a layer of solid lunar regolith during JHCW operation (see Section 1.5).

The methodology for estimating reactor power and mass is presented in Sections 6 and 6, respectively. The mass, power, and performance estimates are given for a range of oxygen production levels in Section 7. The effects of several design variables, including operating temperature, batch time, regolith type/composition are explored. The cost of designing a reactor with a degree of operational flexibility is also presented.

2. Regolith Throughput Requirements

To calculate the amount of regolith that must be processed to meet the oxygen production level, the MRE reactor model sums the contribution from each oxide, taking into account that one might electrolyze only a portion (or none) of certain oxides. The amount of oxygen extracted per kilogram regolith, termed the "oxygen extraction efficiency" (η_{O_2}), is calculated as:

$$\eta_{O_2} \triangleq \frac{m_{O_2}}{m_{regolith}} = \sum_i (w_i) \left(\frac{MW_{O_2}}{MW_{oxide,i}} \right) (r_{mol,i})(e_{frac,i}), \tag{1}$$

where m_{O_2} is the mass of oxygen produced, $m_{regolith}$ is the mass of regolith processed, w_i is the weight percent of oxide i in lunar regolith from Schreiner et al. (2016), $MW_{oxide,i}$ is the molecular weight of oxide specie i, $r_{mol,i}$ is the

number of moles of oxygen in one mole of oxide i, and $e_{frac,i}$ is the fraction of oxide i that is electrolyzed in each batch.

The fraction of each specie that can be electrolyzed ($e_{frac,i}$) is dependent upon the operating temperature, because the liquidus temperature of molten regolith generally increases as the composition changes during electrolysis. Figure 2 shows the liquidus temperature throughout the batch electrolysis calculated using phase diagrams from Slag Atlas (Eisenhüttenleute, 1995). As depicted in the top plot, after FeO is reduced, the liquidus temperature increases as SiO_2 is reduced. After SiO_2, the reduction of MgO and TiO_2 leads to a general decrease in liquidus temperature. Finally, as Al_2O_3 is reduced the liquidus temperature first decreases and then increases to a plateau for a mixture dominated by CaO.

The bottom plot in Figure 2 compares the liquidus temperature curves for Mare and Highlands lunar regolith, which vary due to differences in composition. Although the Highlands regolith has a higher liquidus temperature early in the batch, the liquidus temperature for Mare regolith quickly rises above that of Highlands. This is due to the fact that Mare regolith has more MgO while Highlands regolith has more Al_2O_3.

The batch electrolysis is allowed to progress until the liquidus temperature comes within a 50K safety margin of the operating temperature. As an example, with an operating temperature of 1900K, the reactor can electrolyze approximately 1/2 of the SiO_2 for High-Ti Mare regolith (0.19 kg O_2/kg regolith) and Highlands regolith (0.13 kg O_2/kg regolith) before needing to insert fresh regolith into the reactor to lower the liquidus temperature. If the operating temperature is raised to 2100K, the reactor can now electrolyze 5/6 of the SiO_2 for High-Ti Mare (0.24 kg O_2/kg regolith), and all of the SiO_2, MgO, and TiO_2 for Highlands regolith (0.35 kg O_2/kg regolith). For High-Ti Mare, temperatures above 2200K would be required to open up the possibility of electrolyzing MgO, TiO_2, and some amount of Al_2O_3. Thus, higher operating temperatures increase the oxygen extraction efficiency by allowing the reactor to extract more oxygen per kilogram regolith. For all species, $e_{frac,i}$ is set to a maximum of 0.95 to account for the fact that when the concentration of a particular specie becomes too low, the specie will no longer be preferentially electrolyzed in favor of more abundant species.

Using the fraction electrolyzed ($e_{frac,i}$) of each oxide in lunar regolith, the

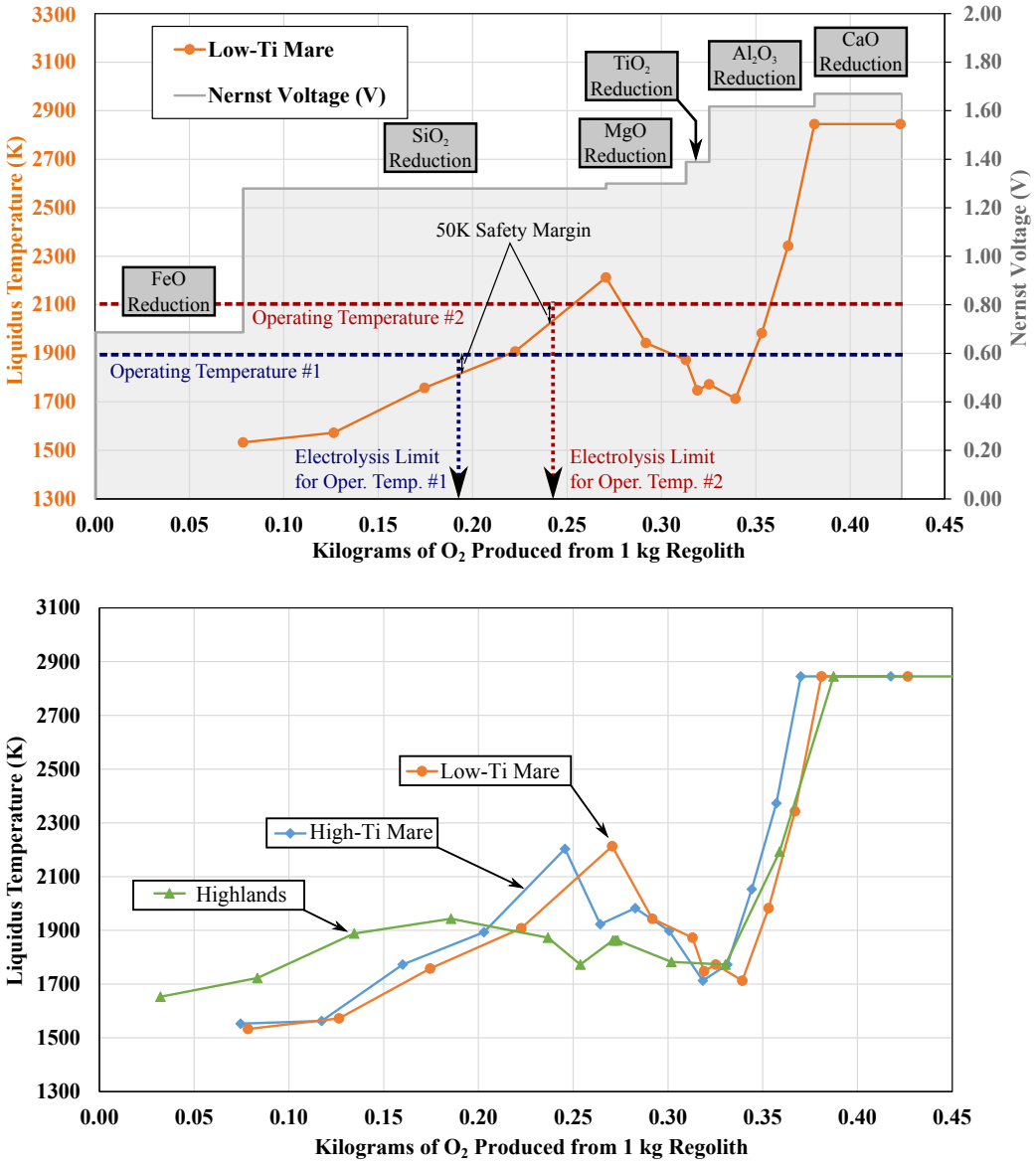

Figure 2: As electrolysis progresses, the composition and properties of the molten regolith vary. *(left)* The liquidus temperature, calculated from Slag Atlas (Eisenhüttenleute, 1995), and the Nernst decomposition potential for Low-Ti Mare lunar regolith initially increase as electrolysis progresses. As the operating temperature increases, the electrolysis can proceed farther to the right in the plot. *(right)* Highlands regolith initially has a higher liquidus temperature, but as electrolysis progresses the liquidus temperature for Mare regolith rises dramatically higher.

amount of molten metal produced can also be calculated:

$$m_{metal,i} = (m_{regolith})(w_i)\left(\frac{MW_{metal,i}}{MW_{oxide,i}}\right)(e_{frac,i}), \tag{2}$$

where $m_{metal,i}$ is the mass of metal produced from oxide i and $MW_{metal,i}$ is the molecular weight of the product metal i. To determine $m_{regolith}$, one can use Equation (1) if oxygen is the primary product or Equation (2) if a particular metal is the primary product.

3. Electrochemistry

The MRE reactor model employs a number of equations to predict the electrochemical performance of the reactor. Faraday's law (Faraday, 1834), with an adjustment for the expected current efficiency, is used to calculate the number of coulombs (C) required to produce a given mass of oxygen:

$$C = (n_{O_2})\left(\frac{nF}{\bar{\eta}_I}\right) = \left(\frac{m_{O_2}}{MW_{O_2}}\right)\left(\frac{nF}{\bar{\eta}_I}\right), \tag{3}$$

where n_{O_2} is the desired moles of oxygen, n is the number of electrons required per diatomic oxygen molecule (=4), F is Faraday's constant, and $\bar{\eta}_I$ is the average current efficiency. Using Equation (1) to substitute for $\left(\frac{m_{O_2}}{MW_{O_2}}\right)$ and including the oxide-specific current efficiencies in the summation yields:

$$C = (m_{regolith})(nF)\sum_i \frac{(w_i)(r_{mol,i})(e_{frac,i})}{(MW_{oxide,i})(\eta_{I,i})}, \tag{4}$$

where $\eta_{I,i}$ is the current efficiency of oxide i.

From experimental work conducted at MIT, the expected current efficiency while electrolyzing iron-bearing molten mixtures is 30-60% (Sirk et al., 2010) due to the redox cycling of multivalent iron ions (Aiken, 1906). As a conservative estimate, the lower bound of 30% was used for FeO. A current efficiency of 50% was used for TiO_2 due to a similar redox cycling phenomena (Chen et al., 2000). Na_2O, P_2O_5, K_2O, and MgO may form gaseous products when electrolyzed (Lindstrom and Haskin, 1979; Sirk et al., 2010), which will likely recombine with some of the product O_2 gas within or above the melt. This can produce a cyclic behavior, so an estimated current efficiency of 50% is used (though this affect can be mitigated with an anode collection tube (Sirk et al., 2010)). For all other species in lunar regolith, a

current efficiency of close to 100% can be expected (Sibille et al., 2010). As a conservative estimate, a value of 95% is used.

Using the number of coulombs predicted by Equation (4), the average current (I_{avg}) can be calculated:

$$I_{avg} = \frac{C}{(t_{batch} - t_{feed})}, \tag{5}$$

where t_{batch} is the total batch time and t_{feed} is a 5 min downtime between each batch during which electrolysis is not performed, to be conservative.

The model assumes that the reactor will be operated in a constant power mode to minimize peak power. Constant power is achieved by varying the current (with an average value of I_{avg}) as the voltage changes due to different species being electrolyzed and the conductivity of the melt changing throughout the batch. For instance, the predicted operating voltage is around 1.85 V for FeO and 3.45 V for SiO_2. The respective operating current for these two species is 1300 A and 700 A. Both of these operating conditions result in a power consumption of approximately 2.4 kW.

4. Multiphysics Simulation

A multiphysics simulation of an MRE reactor, presented in Schreiner et al. (2015), was developed to better understand the complex electro-thermodynamic requirements imposed on an MRE reactor due to the joule heated, cold wall (JHCW) constraint (see Section 1.5). Figure 3 shows a cross-sectional side view of an MRE reactor design in the multiphysics simulation, which is rotated around the axis of revolution on the left to generate the 3D reactor design (shown in Figure 1). The rainbow line illustrates the phase transition between the inner core of molten regolith and the solid regolith layer that insulates the reactor walls. Current streamlines in the molten regolith are depicted in black.

There are four primary modes of heat transfer in the simulation: conduction (the blue arrows in Figure 3), surface-to-surface radiation in the upper cavity (magenta arrows), radiation to ambient on the exterior surface (black arrows), and radiation in participating media (red arrows). Radiation in participating media models the emission, absorption, and scattering of radiation within the high temperature translucent regolith (Arndt et al., 1979; Sibille and Dominguez, 2012).

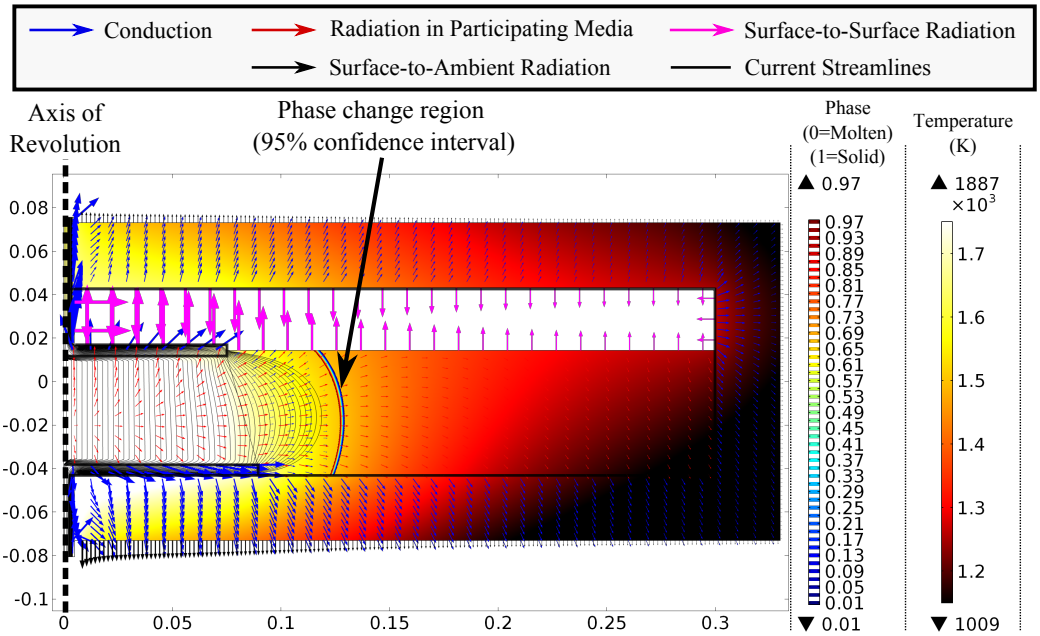

Figure 3: A side view of the cross-section of the multiphysics simulation of a cylindrical MRE reactor. The primary heat fluxes are shown with different colored arrows, scaled by the same factor.

As presented in Schreiner et al. (2015), data on the Enthalpy of Formation, Gibbs Free Energy, specific heat and latent heat of melting for lunar regolith from Schreiner et al. (2016) were leveraged to add heatsinks for the endothermic chemical electrolysis and the heating of newly added regolith in molten region. The constant power operational concept mentioned in the previous section means that regardless of which oxide specie is currently being reduced, the reactor should behavior similarly from a thermal perspective. This means that the the time-varying performance of the reactor should not significantly differ from the steady-state simulation.

5. Using the Simulation to Guide Reactor Design

There are four primary criteria that must be satisfied by an MRE reactor design. The first two, the molten mass and current in the reactor, are derived from the oxygen production level using Equations (1) and (5), respectively. The third, operating temperature, is set as a model input. The fourth criteria is that the design can sustain JHCW operation (see Section 1.5). To

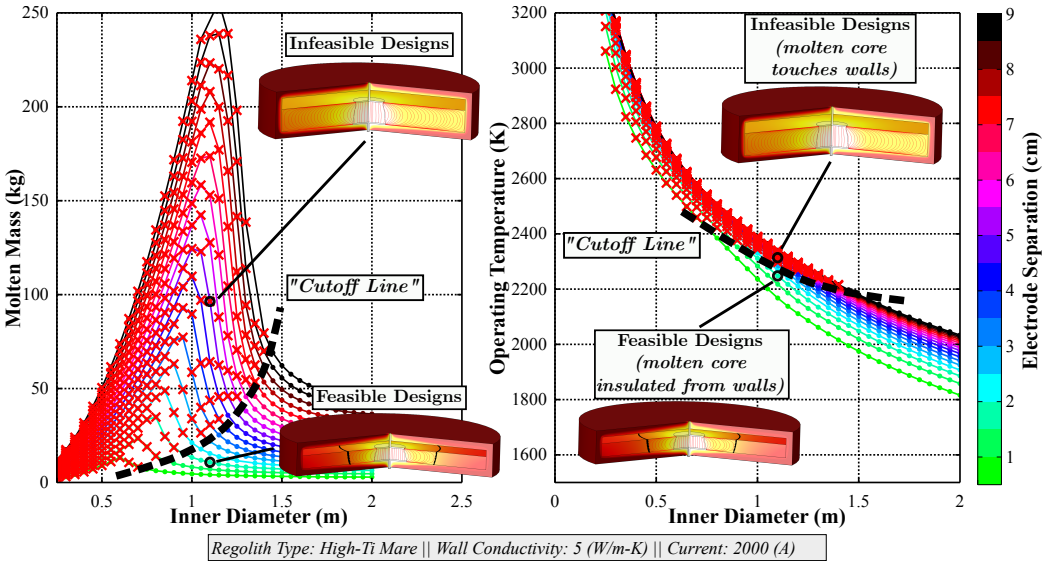

Figure 4: The molten mass in an MRE reactor (left) and the operating temperature (right) depend on reactor diameter and electrode separation. Red X's indicate infeasible designs with the side wall temperature too close to the melting temperature of regolith (1500K).

meet these four performance criteria, the reactor diameter, wall thermal conductivity, and electrode separation must be carefully designed. This section gives an overview of a novel design methodology developed to address this design challenge.

5.1. Effects of Molten Mass and Operating Temperature: The Cutoff Line

The multiphysics simulation described in Section 4 was leveraged to generate a database of over 100,000 reactor designs (consisting of unique combinations of reactor diameter, electrode separation, wall thermal conductivity, current, and regolith feedstock type) with associated performance characteristics (molten mass within the reactor, operating temperature, and whether or not the JHCW condition was satisfied). Figure 4 shows a small sample of the data for the mass of molten regolith in the reactor (left) and operating temperature (right) for a current of 2 kA and a wall thermal conductivity of 5.0 W/m-K, where each line represents a different electrode separation.

The molten mass on the left of Figure 4 first rises with the diameter squared because all of the regolith within the reactor is molten. Beyond a certain inflection point, as reactor diameter increases solid regolith begins

forming at the outer wall of the reactor, decreasing the mass of molten regolith in the reactor as discussed by Schreiner (2015).

As described in Schreiner et al. (2015), data points in Figure 4 with a red "X" overlaid represent infeasible designs, in which the wall temperature rises above 1400K and becomes too close to the melting temperature of lunar regolith circa 1500K. Lower cutoff temperatures were evaluated by Schreiner (2015) and found to be less optimal in terms of both reactor mass and power. The reactor design is chosen using the line that separates infeasible and feasible designs, termed the "cutoff line" as shown in Figure 4. The choice to design reactors on the cutoff lines was made after an initial analysis revealed that those designs had the lowest heat loss per kilogram molten regolith within the reactor (Schreiner, 2015).

5.2. Designing the Electrode Separation

As is evident in the left-hand plot in Figure 4, as the reactor diameter increases the electrode separation must also increase (moving from the green lines towards the black ones) in order to stay on the cutoff line and maintain the joule heated, cold wall constraint. The database generated using the reactor simulation was fit with an empirical equation that describes the appropriate electrode separation for a given reactor design of diameter (D), current (I) and wall thermal conductivity (k_{wall}):

$$\Delta e = e_1 \, I^{e_8} \, (k_{wall})^{e_7} \, \exp\left(\frac{e_3 \, (D - e_2)}{I^{e_5} \left(\frac{e_4}{k_{wall}} + 1 \right)^{e_6}} \right), \tag{6}$$

where e_i are regression coefficients (shown in Table 1) that depend upon regolith type.

Table 1: The regression coefficients for Equation 6, which predicts the appropriate electrode separation needed to maintain thermal equilibrium in an MRE reactor.

Regolith	e_1	e_2	e_3	e_4	e_5	e_6	e_7	e_8
Highlands	0.0011	-0.1945	2.5738	0.6487	0.4656	0.3522	0.0570	0.4348
Mare	0.0008	-0.0458	4.6638	1.3147	0.5827	0.3243	0.0064	0.5857

The electrode separation scaling equation (Equation (6)) is plotted in Figure 5 against a small sample of the data from the multiphysics simulation. It is clear that the electrode separation increases with reactor diameter, decreases with current (left plot), and increases with wall thermal conductivity

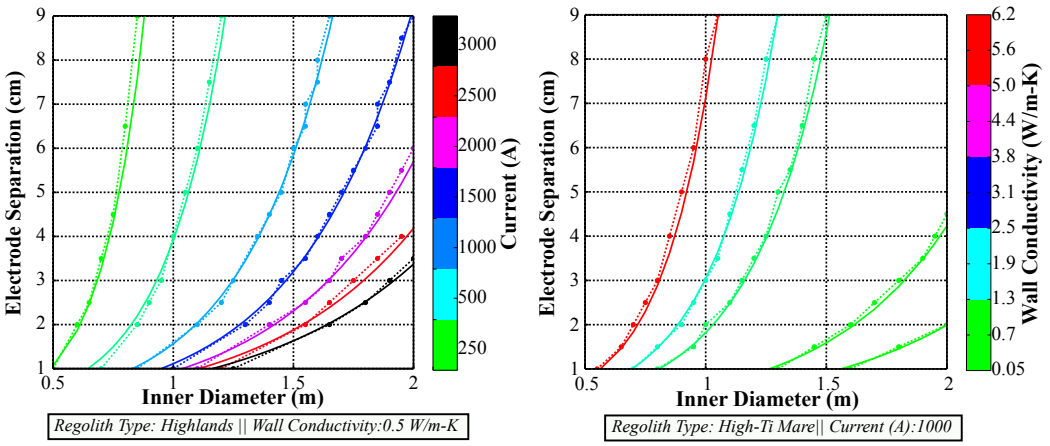

Figure 5: The required electrode separation for a given reactor design. The electrode separation is affected by current (left) and wall thermal conductivity (right). A regression model, illustrated by the solid line, was fit to the multiphysics data, depicted by the data points connected by dashed lines (R^2=0.975, RMSE=0.0032 m).

(right plot) to ensure that the reactor does not generate too much heat and violate the joule heated, cold wall constraint (see Section 1.5).

5.3. The effect of current and wall thermal conductivity on the cutoff lines

It is critical to note that the cutoff lines illustrated in Figure 4 are for a fixed current and wall conductivity. As shown in Figure 6, the cutoff lines are also affected by current (top row) and wall thermal conductivity (bottom row). Current has a minimal effect on the molten mass within the reactor, because as current increases, the required electrode separation decreases to maintain the joule heated, cold wall constraint as discussed in Section 5.2. Reducing the wall thermal conductivity requires a larger reactor diameter to contain a given mass of molten regolith within the reactor. For example, a molten mass of 5 kg can either be met by a reactor with (D = 0.45m and k_{wall} = 5.0 W/m-K) or (D = 1.35m and k_{wall} = 0.05 W/m-K).

Operating temperature increases with reactor current due to the increase in resistive heating within the molten core. Increasing the wall thermal conductivity increases the operating temperature because the electrodes can now be farther apart (see Figure 5) and generate more heat.

5.4. Bounds on Reactor Diameter and Electrode Separation

The cutoff lines in the top row of Figure 6 prove useful for defining bounds on the reactor design, as shown in Figure 7. Succinctly, **1)** the molten mass

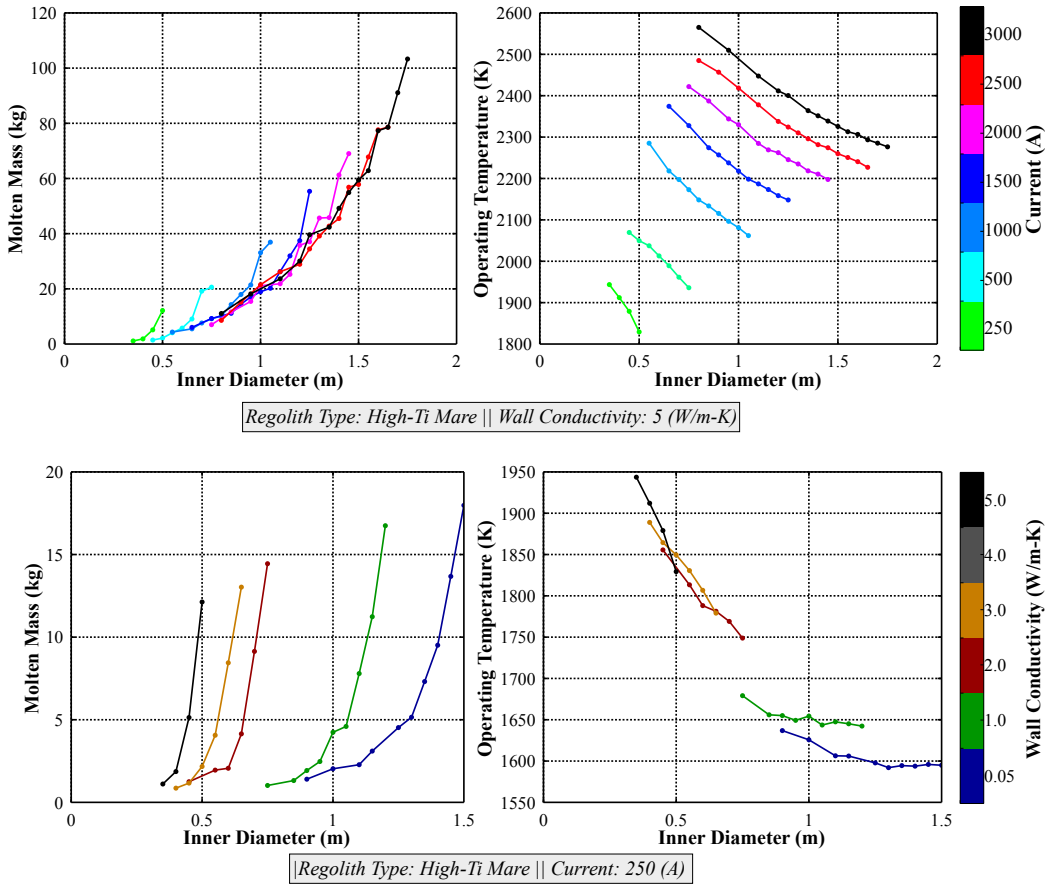

Figure 6: The current and wall thermal conductivity of the reactor affect the cutoff lines that separate infeasible and feasible reactor designs.

requirement sets a minimum feasible reactor diameter, D_{min}, **2)** the operating temperature sets a maximum feasible reactor diameter, D_{max}, and **3)** D_{max} and D_{min} depend on the reactor current and the wall thermal conductivity. The cutoff line represents the minimal reactor diameter that can meet the required amount of molten mass in the reactor while ensuring that no molten regolith touches the reactor wall (left plot in Figure 7). As shown in Figure 4, decreasing the reactor diameter (to the left of the cutoff line) crosses into the infeasible region, meaning that molten regolith will touch the reactor wall.

As can be seen in the right plot Figure 7, the cutoff line represents the maximum reactor diameter that can meet the required operating temperature in the reactor while ensuring that no molten regolith touches the reactor wall.

As shown in Figure 4, increasing the diameter to the right of the cutoff line crosses into the infeasible region, meaning that molten regolith will touch the reactor wall.

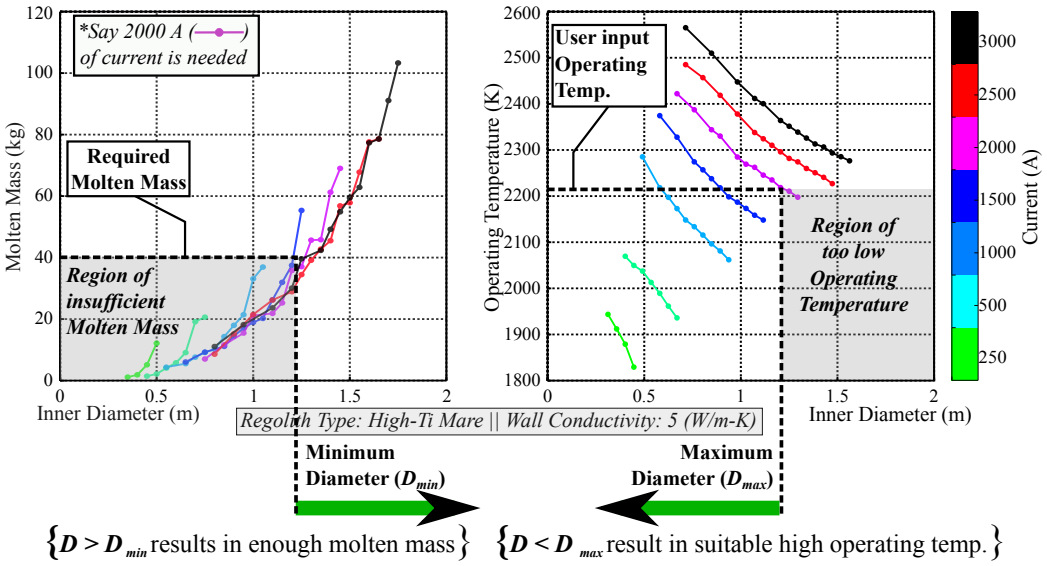

Figure 7: The molten mass (left) and operating temperature (right) as a function of reactor diameter when designed on the cutoff line between infeasible and feasible designs. The minimum and maximum diameter bounds, resulting from the molten mass and operating temperature constraints respectively, are depicted.

As an example, consider a scenario in which 40 kg of molten mass in the reactor and a current of 2 kA are required to meet the desired oxygen production level and the user desires an operating temperature of 2200 K. The 40 kg of molten mass imposes a minimum reactor diameter of about 1.2 m for a current of 2 kA (from the left plot in Figure 7). The 2200 k operating temperature imposes a maximum feasible diameter of about 1.4 m for a current of 2 kA (from the right plot in Figure 7). These bounds can then be adjusted by varying the thermal conductivity of the reactor wall.

The molten mass and operating temperature data from the multiphysics simulation (of which only a small portion is shown in Figures 4 through 7) were fit with empirical regression equations to predict the molten mass (MM)

and operating temperature (T_{op}) for a given reactor design:

$$MM = f(D, I, k_{wall}) = I^{m_6}\, m_4 \exp\left(\frac{m_1\ (D - m_5)}{I^{m_3}\ \left(m_2 + \frac{1}{k_{wall}+0.15}\right)}\right), \quad \text{and} \tag{7}$$

$$T_{op} = f(D, I, k_{wall}) = t_1 + I^{t_5}\, t_2 \exp\left(-\frac{t_3\ (D - t_7)}{I^{t_6}\ \left(1 + \frac{t_4}{k_{wall}+0.15}\right)}\right), \tag{8}$$

where m_i and t_i are regression coefficients which depend upon the type of regolith as shown in Table 2. Equations (7) and (8) can then be algebraically manipulated to derive expressions for the minimum and maximum diameter bounds illustrated in Figure 7:

$$D_{min} = m_5 + \frac{I^{m_3}}{m_1}\left(log\left(\frac{MM}{m_4}\right) - m_6\, log(I)\right)\left(m_2 + \frac{1}{k_{wall}\ +\ 0.15}\right) \tag{9}$$

$$D_{max} = t_7 - \frac{I^{t_6}}{t_3} log\left(\frac{T_{op} - t_1}{I^{t_5}\, t_2}\right)\left(1 + \frac{t_4}{k_{wall} + 0.15}\right) \tag{10}$$

Table 2: The regression coefficients for Equations 7 and 8, which predict the molten mass and operating temperature for an MRE reactor using data from the multiphysics simulation.

Regolith	m_1	m_2	m_3	m_4	m_5	m_6
Highlands	11.04	5.313	0.1598	4.987	0.3429	0.4352
Mare	9.732	3.975	0.2263	5.605	0.4999	0.4853

Regolith	t_1	t_2	t_3	t_4	t_5	t_6	t_7
Highlands	1525	5387	0.3511	-0.02890	0.01048	0.2146	-5.088
Mare	1598	2200	0.5928	-0.04341	0.03897	0.4192	-1.538

5.5. Ensuring Operational Flexibility: The Design Margin

To ensure that a particular design has operational flexibility, a new design variable was introduced, termed the "design margin" (Φ):

$$\Phi \triangleq \frac{D_{max}(T_{op}, I, k_{wall})}{D_{min}(MM, I, k_{wall})}, \tag{11}$$

which represents the ratio of the maximum diameter bound to the minimum diameter bound. Imposing the constraint that $\Phi \geq 1$ ensures that the diameter bounds are properly ordered and $\Phi = 1$ corresponds to diameter bounds that are equal, in which only a single value for reactor diameter results in a feasible design.

Due to the fact that the operating temperature (T_{op}) is set by the user, and the molten mass (MM) and current (I) are fixed for a given oxygen production level (via Equations (1) and (5), respectively), the thermal conductivity of the wall is the only free parameter in Equation (11). By substituting Equations (9) and (10) into Equation (11), a closed-form expression for the required wall thermal conductivity can be derived (shown in Equation (12)):

$$k_{wall} = \frac{I^{m_3}\,\Phi\,m_6\,t_3\,log(I) - I^{t_6}\,m_1\,t_4\,log\left(\frac{T_{op}-t_1}{I^{t_5}\,t_2}\right) - I^{m_3}\,\Phi\,t_3\,log\left(\frac{MM}{m_4}\right)}{\beta},$$

$$where\,\beta \equiv I^{t_6}\,m_1\,log\left(\frac{T_{op}-t_1}{I^{t_5}\,t_2}\right) - m_1\,t_3\,t_7 + \Phi\,m_1\,m_5\,t_3\,\ldots$$

$$\ldots + I^{m_3}\,\Phi\,m_2\,t_3\,log\left(\frac{MM}{m_4}\right) - I^{m_3}\,\Phi\,m_2\,m_6\,t_3\,log(I) - 0.15, \tag{12}$$

The thermal conductivity prescribed by Equation (12), with the maximum diameter from Equation (10), **1)** satisfies the molten mass, current and operating temperature constraints **2)** sets the maximum and minimum diameter bounds within a certain range of one another as specified by the design margin, **3)** ensures that the reactor can support JHCW operation (no molten regolith touches the reactor wall).

5.6. Determining Wall Thickness and MLI Design

In the MRE reactor model, the wall thickness and number of layers of multilayer insulation (MLI), rather than the thermal conductivity of the wall, are the design variables. The MRE reactor is designed such that the thermal resistance of the reactor with real refractory and insulation materials is equivalent to the thermal resistance of the 3 cm thick cylinder in the multiphysics simulation with the thermal conductivity from Equation (12) and the maximum diameter from Equation (10). The total thermal resistance of the reactor includes the thermal resistance from the inner reactor wall to the

outer reactor wall ($R_{cylinder}$) and the thermal resistance associated with radiating heat from the reactor outer surface through layers of MLI to a distant ambient temperature ($R_{radiation}$) (Kreith et al., 2010):

$$R_{total} = R_{cylinder} + R_{radiation}, \tag{13}$$

where:

$$R_{cylinder} = \frac{1}{\pi k_{effective}} \left(\frac{(2(D_{in}/2 + \Delta x)^2)}{\Delta x} + \frac{2\,(H_{in} + 2\Delta x)}{\ln\,(1 + \frac{2\Delta x}{D_{in}})} \right)^{-1}, \tag{14}$$

$$R_{radiation} = (\epsilon^* \sigma (T_{out}^2 + T_\infty^2)\,(T_{out} + T_\infty)\,A)^{-1}, \tag{15}$$

where $k_{effective}$ is the effective thermal conductivity of the combined refractory and insulation layers, Δx is the thickness of the combined insulation and refractory layers, D_{in} is the inner diameter, H_{in} is the inner height of the cylinder, T_{out} is the temperature on the outer surface of the reactor (inside of the MLI layers), T_∞ is the ambient temperature, taken to be 298K, A is the outer surface area of the reactor, σ is the Stefan-Boltzmann constant, and ϵ^* is the effective emissivity of the layers of MLI, given by Gilmore and Donabedian (2003):

$$\epsilon^* = \left(\frac{2\,N}{\epsilon_{MLI}} - N - 1 + \frac{1}{\epsilon_1} + \frac{1}{\epsilon_\infty} \right)^{-1}, \tag{16}$$

where N is the number of layers of MLI, ϵ_{MLI} is 0.03 for Mylar (Gilmore and Donabedian, 2003), and ϵ_1 and ϵ_∞ is the emissivities of the reactor outer surface and environment, respectively (taken to be 1.0). Although Gilmore and Donabedian (2003) assert that the theoretical effective emissivity in Equation (16) is a dramatic underestimate, recent work by Hatakenaka et al. (2013) demonstrated a new pin attachment method for MLI that allows for real hardware performance to approach the theoretical predictions of Equation (16).

The temperature on the outer surface of the reactor inside of the MLI layers (T_{out}) was calculated using the knowledge that all of the heat loss ($\dot{Q}_{heat\text{-}loss}$) calculated in Equation (19) must be radiated out of the reactor.

$$T_{out} = \left(\frac{\dot{Q}_{heat\text{-}loss} + A\sigma\epsilon_\infty (T_\infty)^4}{A\sigma\epsilon^*} \right)^{1/4} \tag{17}$$

Using Equations (13) through (17), the required thermal resistance of the reactor is calculated using the wall thermal conductivity from Equation (12) for $k_{effective}$, and the parameters from the multiphysics simulation: 3 cm for the wall thickness (Δx) and 0.05 for the outer wall emissivity (ϵ^*).

With the required thermal resistance as a design target, the MRE reactor model designs a reactor with real insulation and refractory materials to have the same thermal resistance. First a minimum wall thickness, $\Delta x = \Delta x_{min}$, is set as a user input. Experimental hardware at MIT utilized a two-layer crucible with a wall thickness of 1 cm each (Gmitter, 2008), so a minimum wall thickness of 2 cm was used for this study. With the minimal wall thickness, layers of MLI are added in an attempt to meet the required thermal resistance set forth from the multiphysics model. If this fails to achieve the required thermal resistance (the effect of adding layers of MLI has diminishing returns), the wall thickness is also increased to attempt to achieve the required thermal resistance. The mass of the MLI was taken to be 0.02 kg/m^2 per layer (Plachta and Kittel, 2002) with a factor of two to be conservative and account for fasteners and other supporting material.

he refractory material was chosen to be CW Hi Al Kastite C (high alumina)$^{\text{TM}}$ from Allied Mineral Products, Inc.[5], with a density near 2.8 g/cm^3 and a thermal conductivity around 1.44 W/m-K. Aeroguard HD$^{\text{TM}}$ [6] was selected as the insulation material, for its excellent thermal properties at high temperatures and low density of 0.2 g/cm^3.

A thickness ratio of 3:1 (insulation:refractory thickness) was used on the reactor bottom and side walls and 6:1 was used on the reactor top, as the contact between molten regolith and the roof of the reactor will be minimal. The structural thickness is set such that the hoop stress resulting from the operating pressure is less than the yield stress of the material with a safety factor (SF) of 3.5 ($\sigma_y = (SF)\ \left(\frac{Pr}{2t}\right)$).

6. Estimating Reactor Mass and Power

The MRE reactor model estimates reactor mass using the geometry of the reactor described above. An ullage of 1.5 was used, defined as the ratio of inner reactor height to maximum electrode separation. Due to the fact that the

[5] http://www.alliedmineral.com/

[6] http://www.microthermgroup.com/landingpage/assets/TDS_AEROGUARD_V1-EN.pdf

structure may encounter elevated temperatures, titanium was selected over aluminum. With the diameter, height, and thickness of the structural, insulation, and refractory layers determined, the mass of the cylindrical reactor shell are calculated.

The mass of the anode and cathode are also taken into account in the MRE reactor model. The diameter of the cathode plate is fixed at 15% of the reactor diameter, after an initial analysis revealed that this ratio provided a good balance between larger molten masses and higher operating temperatures. The anode diameter is designed to be 19% less than the cathode diameter, using the same ratio as Sibille and Dominguez (2012). The cathode and anode shafts are designed to be long enough to pass through the reactor wall. The diameters of the anode and cathode shafts are set to 2 cm plus $\frac{1}{25}^{\text{th}}$ of the plate diameter. The mass of the anode and cathode are then calculated using these dimensions.

As mentioned in Section 4, half of the regolith heating power is provided by a preheater that bakes out volatiles and warms up fresh regolith. The mass of this preheater was calculated using trends from a handbook on electric resistive heaters (Omega, 1995).

The total reactor power is estimated using the sum of four different terms:

$$P_{total} = \dot{Q}_{regolith\text{-}heatup} + P_{(\Delta G)} + \dot{Q}_{endothermic} + \dot{Q}_{heat\text{-}loss} \tag{18}$$

The power required to heat the regolith from ambient temperature (∼300K) to the operating temperature ($\dot{Q}_{regolith\text{-}heatup}$), is calculated using the specific heat and latent heat of melting for lunar regolith from Schreiner et al. (2016). The heat required to offset the endothermic electrolysis reaction ($\dot{Q}_{endothermic}$) is calculated using the difference between the Enthalpy of Formation and Gibbs Free Energy averaged over all of the oxide species electrolyzed, using the thermochemical data from Schreiner et al. (2016). The power required to perform the electrolysis chemical reaction is calculated using the Gibbs Free Energy averaged over all of the oxide species electrolyzed during a given batch.

The radiative heat loss to the environment ($\dot{Q}_{heat\text{-}loss}$) is predicted using regression equations that were fit to the data from the multiphysics simulation ($R^2 = 0.997$, RMSE = 0.51kW):

$$\dot{Q}_{heat\,loss} = h_1 \left(\frac{\exp\left(\frac{h_2}{D+h_3}\right)}{h_4 + \frac{1}{k_{wall}-h_6}} \right) + h_5\, k_{wall} \tag{19}$$

where h_i are regression coefficients given in Table 3 which depend upon the regolith type.

Table 3: The regression coefficients for Equation 19, which predicts the expected heat loss from an MRE reactor based off of data from the multiphysics simulation.

Regolith	h_1	h_2	h_3	h_4	h_5	h_6
Highlands	1.591E+06	-8.289	1.083	1.146	222.4	-0.03572
Mare	1.756E+06	-8.843	1.165	1.135	188.9	-0.03446

Figure 8 shows data generated by the multiphysics simulation (dashed lines with data points) and the predictions of Equation (19) (solid lines). Current does not significantly affect the heat loss for a fixed diameter reactor, because the electrode separation decreases as current increases to maintain the joule heated, cold wall constraint (see Section 1.5), as shown in Figure 5. From Figure 8, we see that for a fixed diameter, the thermal topology required by the joule heated, cold wall condition imposes a certain heat loss on the reactor which does not significantly depend on the current.

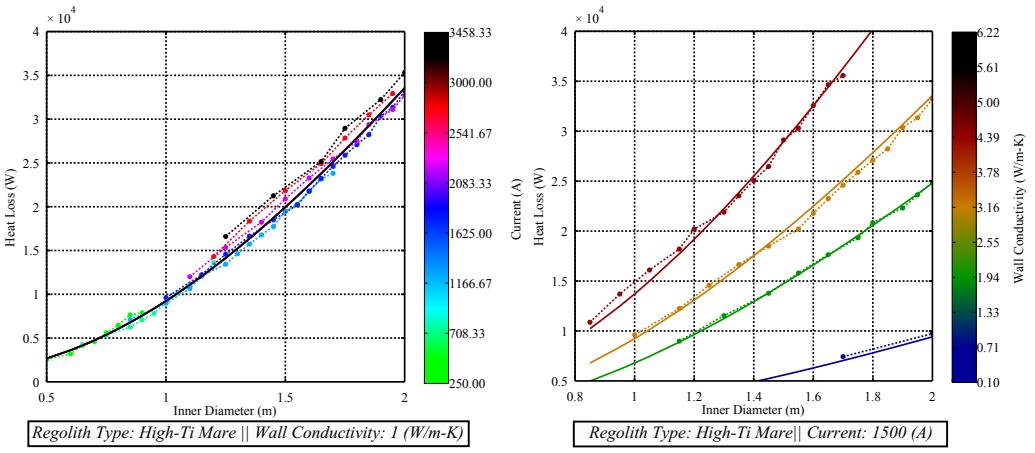

Figure 8: The heat loss does not significantly depend on current (left), but is affected by wall thermal conductivity (right) when designing on the cutoff lines. A nonlinear regression model (solid lines) was fit to the data from a multiphysics simulation (dots with dashed lines) with R^2=0.997, RMSE=0.51kW.

Conversely, the heat loss does appear to depend significantly on the wall thermal conductivity, with a lower wall thermal conductivity intuitively resulting in less heat loss. The observed decrease in heat loss with decreasing

wall thermal conductivity is a direct result of the decrease in electrode separation observed in Figure 5.

7. Results: MRE Reactor Performance and Design Trends

7.1. Oxygen Extraction Efficiency and Current Efficiency

The oxygen extraction efficiency (η_{O_2}), is defined as the number of kilograms of oxygen that can be extracted per kilogram regolith, as defined in Equation (1). Figure 9 shows how η_{O_2} increases with operating temperature for three types of lunar regolith. Using composition data from Schreiner et al. (2016), the maximum value for η_{O_2} is 0.454 for Highlands, 0.417 for High-Ti Mare, and 0.423 for Low-Ti Mare regolith.

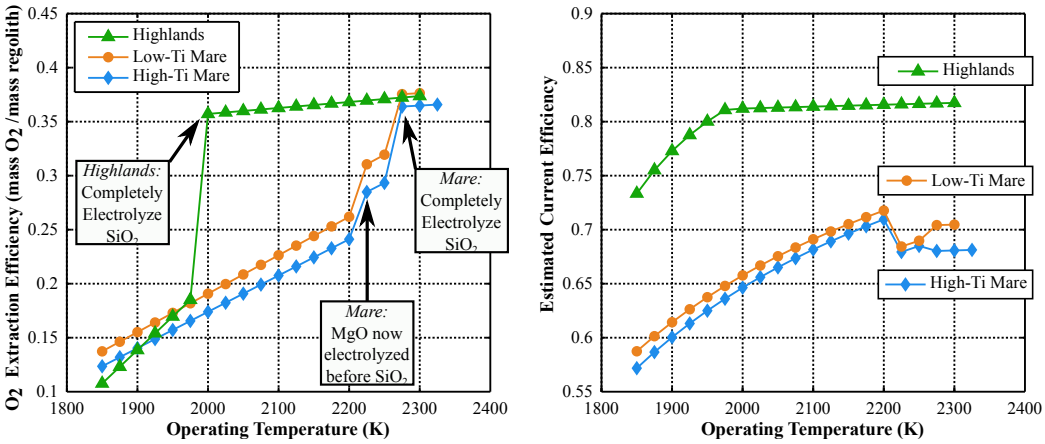

Figure 9: The oxygen extraction efficiency (left) and current efficiency (right) estimates for an MRE reactor.

As discussed in Section 2, higher operating temperatures allow one to reduce more of the oxides in lunar regolith before the melting temperature of the molten regolith core approaches the operating temperature, causing the core to risk solidification and reactor shutdown. Thus by raising the operating temperature, one can extract more oxygen per kilogram regolith and increase η_{O_2}.

For Highlands regolith, η_{O_2} exhibits a sharp rise around 2000K, at which point the reactor can reduce all of the SiO_2 (see Figure 2: the SiO_2 peak is around 1950K + 50K safety margin = 2000K). For Mare regolith, a jump in η_{O_2} occurs around 2200K. This jump is not due to electrolyzing all of the

SiO_2, but is rather due to a reversal in the electrolysis order of SiO_2 and MgO. As described in Schreiner et al. (2016), the Gibbs Free Energy for MgO rises above that of SiO_2, meaning that MgO will be preferentially electrolyzed over SiO_2 at temperature above 2200K. In reality, it is likely that both MgO and SiO_2 will be concurrently reduced at temperatures near 2200K, but for the MRE reactor model all oxide species are assumed to be discretely reduced in the order of decreasing Gibbs Free Energy for simplicity.

Figure 9 shows how the current efficiency is lower at low operating temperatures due to the relatively large amount of FeO that must be electrolyzed, with a low current efficiency of 30%, to meet the oxygen production level (see Section 3). At higher operating temperatures, more SiO_2 and other species can be electrolyzed with a higher current efficiency, increasing the average current efficiency. For Highlands regolith, (η_I) increases from 74% at an operating temperature of 1850K to 82% above 2000K. For Mare regolith a similar increase is observed from 57% at 1850K to 72% at 2200K. The drop in current efficiency for Mare regolith near 2200K is due to MgO also being electrolyzed, with a low current efficiency of 50% (see Section 3).

One may note that the current efficiency estimates presented here appear lower than many numbers cited in the literature, which are often around 90-100% (Sibille et al., 2010; Vai et al., 2010; Sirk et al., 2010). These estimates are for melts without iron, titanium, or sodium-oxides, which is why the current efficiency is dramatically higher. Realistic current efficiencies over an entire batch, in which FeO, SiO_2, TiO_2, and other oxides may be reduced, will be lower.

7.2. The Effect of Operating Temperature on Mass and Power

Figure 10 shows the how operating temperature affects reactor mass (left) and power (right) over a range of oxygen production levels for High-Ti Mare regolith. Higher operating temperatures increase the oxygen extraction efficiency (see Figure 9), which reduces the regolith throughput requirement and reactor size. Higher operating temperatures also result in a larger temperature drop that must be accommodated before reaching the reactor wall and a lower density for molten regolith. Although these two effects drive larger reactor designs, they are outweighed by the increase in oxygen extraction efficiency and subsequent decrease in reactor size.

At lower temperatures (1850K-2150K), reactor power increases with operating temperature due to the need for a higher temperature drop between

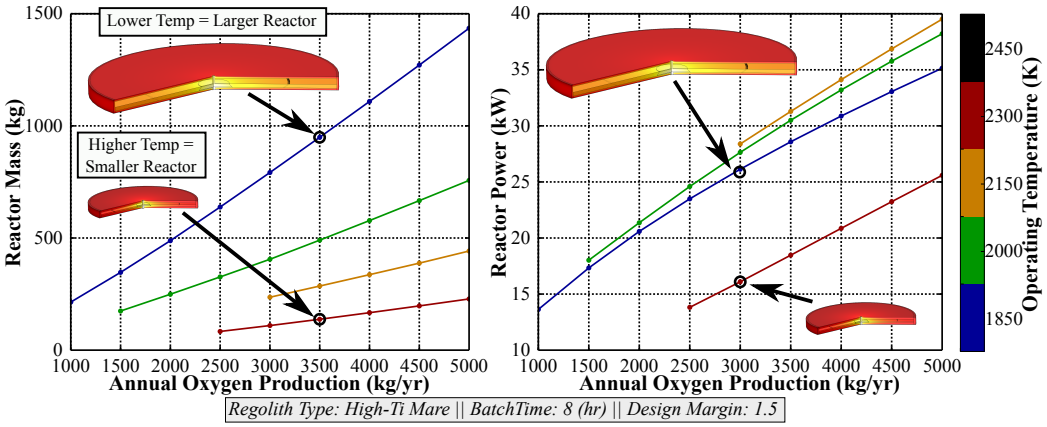

Figure 10: The mass (left) and power (right) for an MRE reactor over a range of oxygen production levels. Each line represents a different operating temperature and all designs have a margin of 1.5.

the reactor core and walls (due to the joule heated, cold wall constraint described in Section 1.5). At higher temperatures, this effect is outweighed by the steep increase in oxygen extraction efficiency around 2200K (as seen in Figure 9 for High-Ti Mare) and the increase in electrical conductivity which decreases the resistive heating that exits the reactor as heat loss.

Figure 10 also illustrates that a minimum achievable oxygen production level exists. Below a certain oxygen production threshold, the reactor size becomes too small to maintain joule heated, cold wall operation. As operating temperature increases, it becomes more difficult to design a small reactor and the minimum oxygen production threshold increases. For High-Ti Mare above 2200K, this effect is outweighed by the dramatic increase in oxygen extraction efficiency as seen Figure 9, and the minimum oxygen production threshold decreases with increasing operating temperature.

7.3. The Effect of Design Margin on Mass and Power

The trends in operating temperature presented above are for reactor designs with a fixed design margin of 1.5. This means that the wall thermal conductivity is designed such that the maximum diameter set by the operating temperature is 1.5 times the minimum diameter set by the molten mass requirement (see Section 5.5). As seen in Figure 11, increasing the design margin results in higher reactor mass and power, though it does increase the maximum production level for a single reactor.

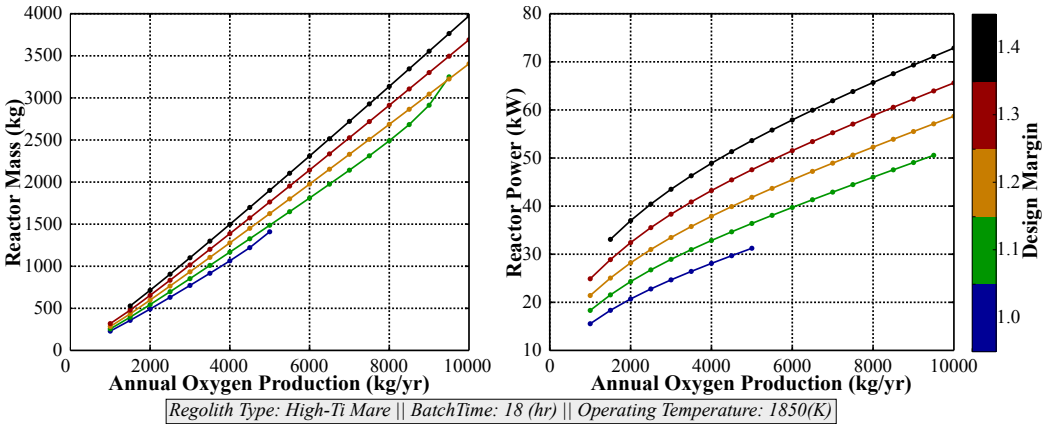

Figure 11: The mass and power of an MRE reactor at an operating temperature of 1850K, where each line shows a different design margin. Larger design margins clearly increase both mass and power, but enable higher production levels.

Perhaps the most important effect of design margin is on the acceptable range of electrode separation values. The design margin controls the acceptable bounds on reactor diameter and because there is a one-to-one mapping between reactor diameter and electrode separation, this also translates into bounds on the electrode separation. The left-hand plot in Figure 12 demonstrates how increasing the design margin enables a range of electrode separations that **1)** generate enough heat to maintain the central molten core and **2)** maintain the joule heated, cold wall operation (no molten material touches the reactor wall) by not generating excessive heat. Having a range of viable electrode separation values will enable a control system to actuate the electrode separation during operation to better control the reactor thermal topology.

The multiphysics simulation (see Section 4) was leveraged to validate the range of electrode separations enabled by a design margin greater than 1. The right side of Figure 12 shows reactor designs with the maximum (top) and minimum (bottom) electrode separations for an oxygen production of 4000 kg O_2/year with a design margin of 1.2. Both reactor designs can support joule heated, cold wall operation by insulating the central molten core from the reactor walls with a layer of solid regolith.

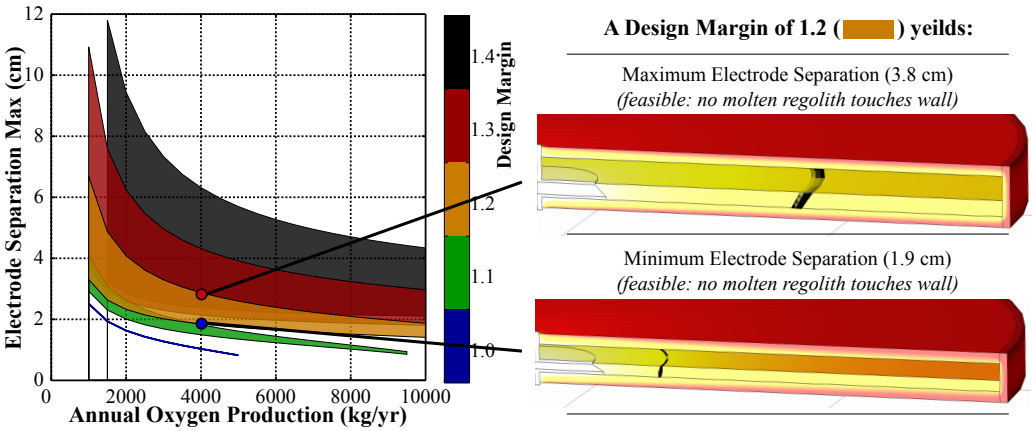

Figure 12: (left) Increasing the design margin opens up a larger range of feasible electrode separation values to enable operational flexibility. (right) At a production level of 4000 kg O_2/year, a design margin of 1.2 enables an acceptable electrode separation range of 1.9 cm to 3.8 cm, validated using the multiphysics simulation.

7.4. The Effect of Regolith Type/Composition on Mass and Power

The MRE reactor model has a strong dependence on regolith type. Of the regolith material properties presented in Schreiner et al. (2016), composition, density, specific heat, electrical conductivity, current efficiency, latent heat of melting, endothermic power, and electrolysis power all depend upon regolith type. Furthermore, different sets of multiphysics data were generated for Highlands and Mare regolith (the differences between High-Ti and Low-Ti Mare were not significant enough to warrant separate runs with the multiphysics simulation). This resulted in separate sets of regression coefficients for the appropriate electrode separation (Table 1), molten mass and operating temperature (Table 2), and heat loss (Table 3).

Figure 13 shows how the regolith type affects the mass and power of an MRE reactor for operating temperatures of 1850K (top row), 2000K (middle row), and 2300K (bottom row). From these results, it appears that the liquidus temperature curves shown in Figure 2 play a large role in the regolith type dependence. That is, the type of regolith strongly affects how much oxygen can be extracted from lunar regolith before having to stop to avoid solidification of the central molten core.

At 1850K (top row of Figure 13), one can extract less oxygen per kilogram Highlands regolith compared to Mare regolith so Highlands reactors must process more regolith, which increases reactor power. Furthermore,

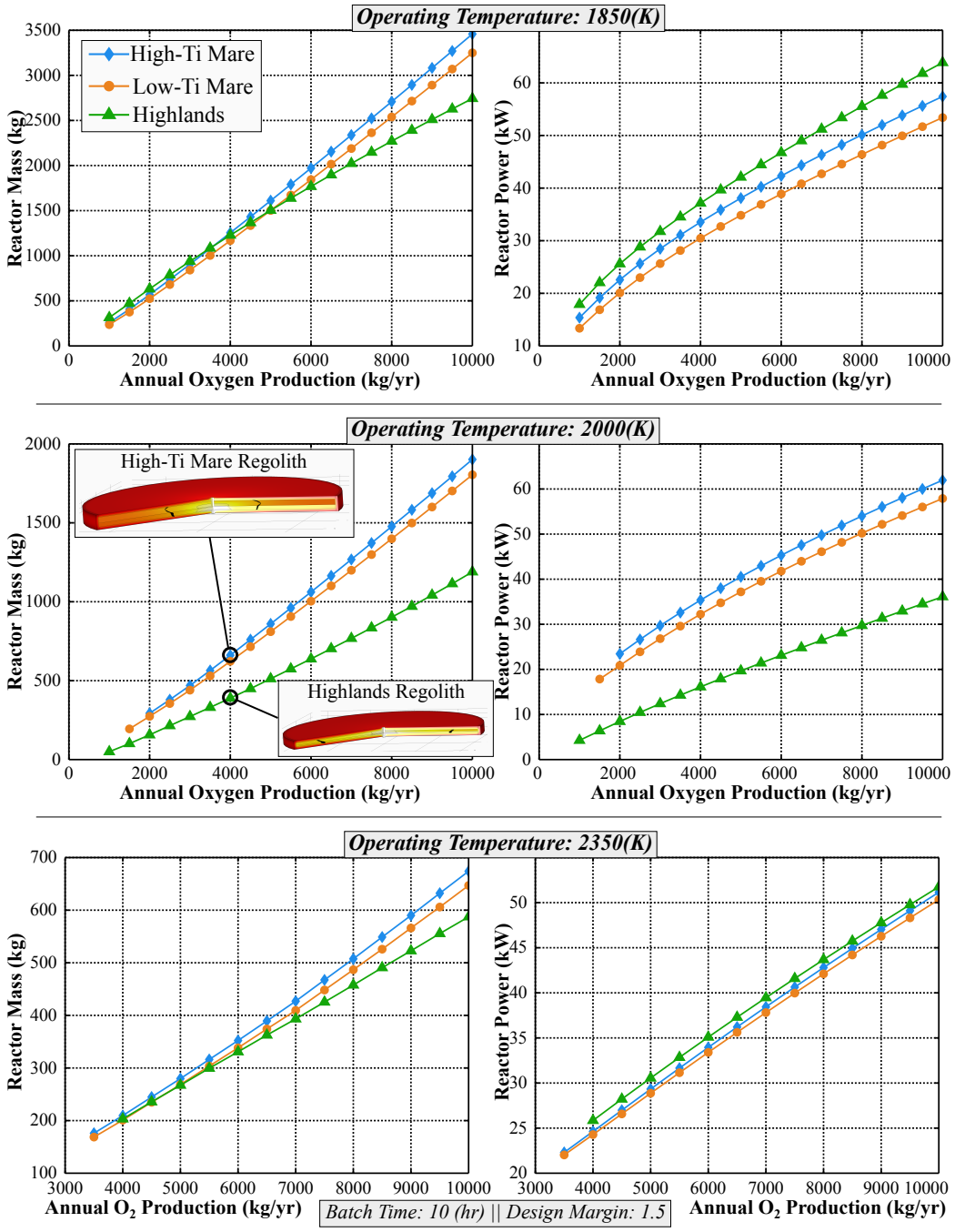

Figure 13: The mass and power of an MRE reactor for three different types of regolith with operating temperatures of 1850K (top), 2000K (middle), and 2300K (bottom).

Highlands regolith has more SiO_2, which must be electrolyzed at a higher voltage than FeO and subsequently drives the power requirement higher. Although Highlands reactors have a higher regolith throughput requirement, reactor mass remains relatively the same between Highlands and Mare regolith because Highlands regolith has a lower electrical conductivity, which results in more resistive heating in the central core and less insulation around the reactor wall.

The trend in liquidus temperature reverses around 2000K (middle row of Figure 13), at which point an MRE reactor can now electrolyze more oxygen from Highlands regolith compared to Mare. This results in a dramatic decrease in reactor mass (33%) and power (60%) for Highlands regolith compared to Mare for operating temperatures circa 2000K. At operating temperatures circa 2300K, the mass and power of MRE reactors is again somewhat similar for both Highlands and Mare reactors. Highlands reactors are slightly less massive at higher production levels but slightly more power intensive, due to more resistive heating and therefore less insulation required.

7.5. The Effect of Batch Time on Mass and Power

In the MRE reactor model, longer batch times require more molten regolith to be held in the reactor during operation. Figure 14 illustrates how longer batch times result in larger reactors that require more power. This is due to the fact that the reactor must now maintain a larger volume of molten material for a longer period of time. Although shorter batch times reduce reactor mass and power, they also clearly limit the maximum production level of a single reactor, as observed in Figure 14.

One attractive option for an MRE reactor is semi-continuous operation, in which regolith is continuously added while molten metals and slag are periodically withdrawn. This study of batch time is still relevant for continuous operation reactors, as it describes the time between molten metal withdrawals and the ratio of molten mass to reactor current. The results shown in Figure 14 demonstrate how lower ratios of molten mass to current (shorter batch times) are optimal, but they limit the production level of the reactor.

7.6. Molten Metal Production

Figure 15 illustrates the estimated metal produced from an MRE reactor, as discussed in Section 2, as a function of operating temperature for Mare (left) and Highlands (right) regolith. As temperature increases, the

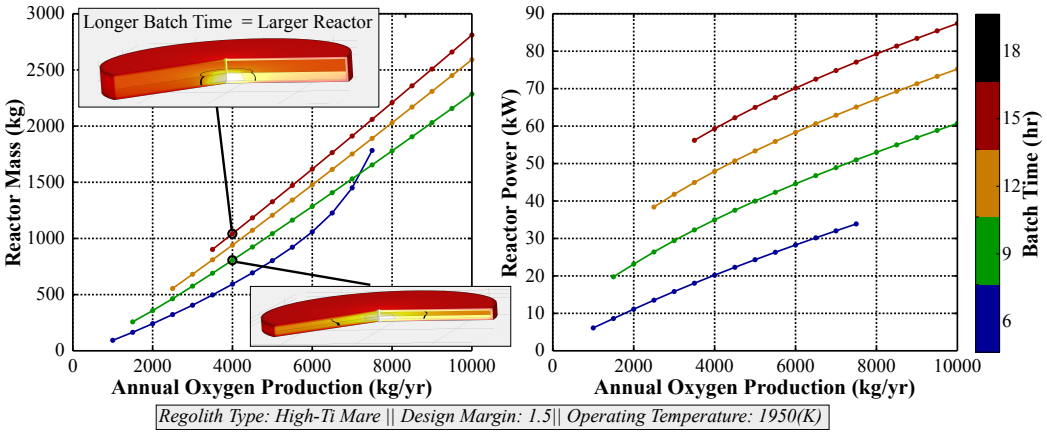

Figure 14: The mass and power of an MRE reactor as a function of oxygen production and batch time. Longer batch times increase reactor mass and power.

metal production increases while the mass of leftover slag decreases by approximately 35% from 1850K to 2300K (for Mare) or 2000K (for Highlands). Reactors processing Highlands regolith can produce aluminum at lower operating temperatures because the liquidus temperature peak occurs around 2000K for Highlands regolith and around 2250K for Mare (see Figure 2). Due to differences in regolith composition (Schreiner et al., 2016), reactors processing Mare regolith can produce more iron and titanium per kilogram regolith, while reactors processing Highlands regolith can produce more silicon and aluminum per kilogram regolith.

The data in Figure 15 is for an oxygen production level of 10,000 kg O_2/year. At higher operating temperatures (>2000K for Highlands and >2300K for Mare), the cumulative amount of metal produced is almost equal to the oxygen production level.

8. Conclusions

We have developed a parametric sizing model for a Molten Regolith Electrolysis reactor to produce oxygen and molten metals from lunar regolith. The reactor model is grounded in a foundation of regolith material property models presented in Schreiner et al. (2016), which are validated using data from Apollo samples and lunar simulants. The oxygen production level drives the regolith throughput requirements and reactor current. A multiphysics simulation of an MRE reactor is developed and utilized to generate

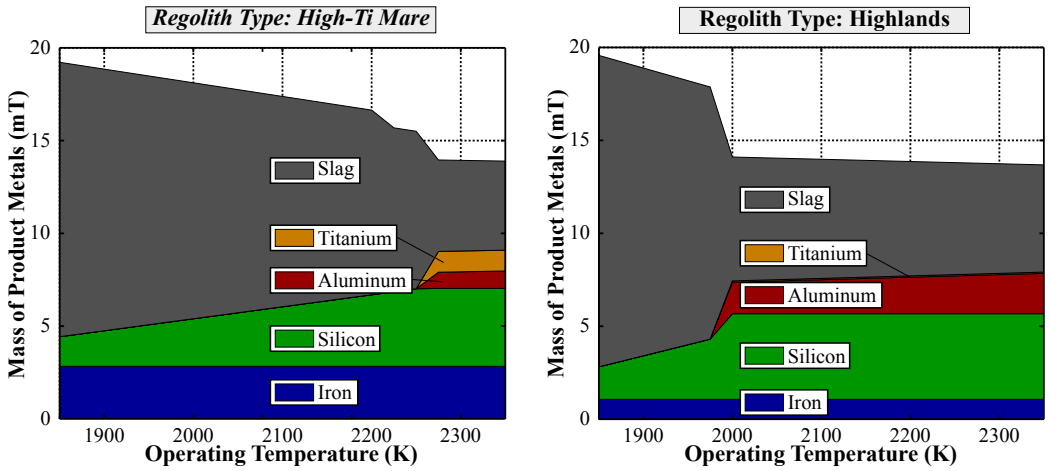

Figure 15: The amount of metal produced by an MRE reactor operating on Mare (left) and Highlands (right) regolith producing 10,000 kg O_2/yr. As operating temperature increases, more oxides can be reduced to produce more molten metal and leave less leftover slag.

a database of reactor designs and performance characteristics. A novel design methodology is developed that leverages this database to parametrically design MRE reactors with mass and power estimates.

The predicted mass and power of an MRE reactor are presented over a range of oxygen production levels and the effects of operating temperature, regolith type, batch time, and design margin (degree of operational flexibility) are explored. Higher operating temperatures appear to always reduce reactor mass and sometimes reduce power (Figure 10), but this effect has a strong dependence on regolith type (Figure 13). Prior to this work it was unclear whether higher operating temperatures would indeed result in smaller reactor sizes due to the mixed effect of operating temperature on regolith material properties and reactor thermal topology. Higher operating temperatures also enable MRE reactors to produce more molten metal per kilogram regolith and open up the possibility of producing aluminum and titanium.

Larger design margins are found to be an effective method for increasing reactor operation flexibility by enabling a range of feasible electrode separations (Figure 12), but come at the cost of increased reactor mass and power. Lower design margins limit the maximum production level of a single reactor (Figure 11). Longer batch times increase reactor mass and power, but open up higher production levels.

These trends reveal the complex nature of MRE reactor design. Many of

the design variable effects are coupled and redundant. For example, longer batch times and higher design margins both increase reactor mass and power. The optimal design variables (operating temperature, batch time, design margin, etc.) strongly depend on one another. Clearly, an optimization scheme must be employed to better understand the optimal MRE reactor design.

Regolith type (and therefore composition) also has an impact on MRE reactor design and performance (Figure 13). For midrange operating temperatures circa 2000K, Highlands reactors are 33% less massive and require 60% less power than Mare reactors. At the low and high ends of the operating temperature design space, Highlands reactors are marginally less massive but require slightly more power.

The model predicts that an MRE reactor is able to produce oxygen with a specific mass and power on the order of ≈0.1 (kg reactor)/(kg O_2/year) and ≈4 (W)/(kg O_2/year), respectively. It is critical to note that these values are for a non-optimized design, one would expect lower values when the design variables are optimized. These values provide initial evidence that an MRE reactor can be a viable option for producing oxygen from lunar regolith to resupply ECLSS consumables and provide oxidizer for chemical propulsion systems. Although these numbers differ from those presented in Schreiner et al. (2015), they represent higher fidelity designs and are therefore considered more accurate.

Despite these promising results, these mass and power predictions are for the MRE reactor alone. The integrated ISRU system must be studied and optimized to understand the total mass and power associated with producing oxygen on the lunar surface.

9. Acknowledgments

This work was supported by a NASA Space Technology Research Fellowship (Grant #NNX13AL76H). Any opinions, findings, and conclusions or recommendations expressed in this material are those of the author and do not necessarily reflect the views of NASA.

References

Aiken, R. H. (1906). Process of making iron from the ore. US Patent 816,142.

Allanore, A., Yin, L., and Sadoway, D. R. (2013). A new anode material for oxygen evolution in molten oxide electrolysis. *Nature*.

Altenberg, B. (1990). Processing lunar in-situ resources. *Technical Research and Development Project Job*. 90634-002.

Arndt, J., Flad, K., and Feth, M. (1979). Radiative cooling experiments on lunar glass analogues. In *Lunar and Planetary Science Conference Proceedings*, volume 10, pages 355–373.

Badescu, V. (2012). *Moon: Prospective Energy and Material Resources*. Springer.

Balasubramaniam, R., Gokoglu, S., and Hegde, U. (2010). The reduction of lunar regolith by carbothermal processing using methane. *International Journal of Mineral Processing*, 96(1):54–61.

Carr, B. (1963). Recovery of water or oxygen by reduction of lunar rock. *AIAA Journal*, 1(4):921–924.

Carroll, W. F. (1983). Research on the use of space resources. *JPL Publication 83-36*.

Chen, G. Z., Fray, D. J., and Farthing, T. W. (2000). Direct electrochemical reduction of titanium dioxide to titanium in molten calcium chloride. *Nature*, 407(6802):361–364.

Chepko, A. (2009). *Technology selection and architecture optimization of in-situ resource utilization systems*. PhD thesis, Massachusetts Institute of Technology.

Colson, R. O. and Haskin, L. A. (1990). Lunar oxygen and metal for use in near-earth space: Magma electrolysis. In *In Arizona Univ., NASA Space Engineering Research Center for Utilization of Local Planetary Resources*, volume 1.

Curreri, P., Ethridge, E., Hudson, S., Miller, T., Grugel, R., Sen, S., and Sadoway, D. (2006). Process demonstration for lunar in situ resource utilizationmolten oxide electrolysis. *NASA Marshall Space Flight Center. MSFC Independent Research and Development Project*. Project No. 5-81.

Diaz, J., Ruiz, B., Blair, B., Harsch, M., Duke, M., Parrish, C., Lueck, D., Mueller, R., and Whitlow, J. (2005). Space transportation architectures and refueling for lunar and interplanetary travel and exploration (starlite). Technical Report NASA Grant NAG9-1535, Center for the Commercial Applications of Combustion in Space, Colorado School of Mines.

Dominguez, J. A., Sibille, L., and Poizeau, S. (2009). Modeling joule heating effect on lunar oxygen generation via electrolytic reduction. In *AIAA 47th Aerospace Sciences Meeting Proceedings on Disc*.

Duke, M. B., Diaz, J., Blair, B. R., Oderman, M., and Vaucher, M. (2003). Architecture studies for commercial production of propellants from the lunar poles. In *AIP Conference Proceedings*, pages 1219–1226. AIP Publishing.

Eisenhüttenleute, V. D. (1995). *Slag Atlas*. Verlag Stahleisen GmbH.

Faraday, M. (1834). Xxv. experimental researches in electricity.seventh series. *The London and Edinburgh Philosophical Magazine and Journal of Science*, 5(27):161–181.

Gilmore, D. G. and Donabedian, M. (2003). *Spacecraft Thermal Control Handbook: Cryogenics*, volume 2. AIAA.

Gmitter, A. J. (2008). *The influence of inert anode material and electrolyte composition on the electrochemical production of oxygen from molten oxides*. PhD thesis, Massachusetts Institute of Technology.

Haskin, L. A., Colson, R. O., Lindstrom, D. J., Lewis, R. H., and Semkow, K. W. (1992). Electrolytic smelting of lunar rock for oxygen, iron, and silicon. In *Lunar Bases and Space Activities of the 21st Century*, volume 1, pages 411–422.

Hatakenaka, R., Miyakita, T., Sugita, H., Saitoh, M., and Hirai, T. (2013). Thermal performance and practical utility of a mli blanket using plastic pins for space use. *American Institute of Aeronautics and Astronautics*, pages 1–11.

Hegde, U., Balasubramaniam, R., and Gokoglu, S. (2009). Development and validation of a model for hydrogen reduction of jsc-1a. *AIAA Proceedings*.

Jarrett, N., Das, S., and Haupin, W. (1980). Extraction of oxygen and metals from lunar ores. *Space Sol. Power Rev.;(United States)*, 1(4).

Joosten, B. K. and Guerra, L. A. (1993). Early lunar resource utilization: a key to human exploration. In *AIAA Space Programs and Technologies Conference, AIAA*, pages 93–4784.

Kesterke, D. G. (1970). Electrowinning oxygen from silicate rocks. *NASA Special Publication*, 229:139.

Kreith, F., Manglik, R., and Bohn, M. (2010). *Principles of heat transfer*. Cengage learning.

Landis, G. A. (2005). Materials refining for solar array production on the moon. *NASA Technical Memorandum*, 214014.

Lindstrom, D. J. and Haskin, L. A. (1979). Electrochemistry of lunar rocks. In *Princeton University and American Institute of Aeronautics and Astronautics, Conference on Space Manufacturing Facilities, 4th, Princeton University, Princeton, NJ, May 14-17, 1979, AIAA 7 p.*, volume 1.

Mason, L. (1992). Beneficiation and comminution circuit for the production of lunar liquid oxygen. *Space*, pages 1139–1149.

Omega (1995). *The Omegalux complete electric heaters handbook and encyclopedia*. Omega Engineering.

Paramore, J. D. (2010). *Candidate anode materials for iron production by molten oxide electrolysis*. PhD thesis, Massachusetts Institute of Technology.

Plachta, D. and Kittel, P. (2002). An updated zero boil-off cryogenic propellant storage analysis applied to upper stages or depots in an leo environment. *AIAA Paper*, 3589:7–10.

Rapp, D. (2007). *Human Missions to Mars*. Springer.

Sacksteder, K. R. and Sanders, G. B. (2007). In-situ resource utilization for lunar and mars exploration. *The 5th AIAA Aerospace Sciences Meeting and Exhibit*.

Schreiner, S. S. (2015). *Molten Regolith Electrolysis Reactor Modeling and Optimization of In-Situ Resource Utilization Systems*. PhD thesis, Massachusetts Institute of Technology.

Schreiner, S. S., Dominguez, J. A., Sibille, L., and Hoffman, J. A. (2016). Thermophysical property models for lunar regolith [tentative]. *Advances in Space Research*. Under Review.

Schreiner, S. S., Sibille, L., Dominguez, J. A., Hoffman, J. A., Sanders, G. B., and Sirk, A. H. (2015). Development of a molten regolith electrolysis reactor model for lunar in-situ resource utilization. *AIAA SciTech Conference - 8th Symposium on Space Resource Utilization*.

Sherwood, B. and Woodcock, G. R. (1993). Cost and benefits of lunar oxygen: Economics, engineering, and operations.

Sibille, L. and Dominguez, J. A. (2012). Joule-heated molten regolith electrolysis reactor concepts for oxygen and metals production on the moon and mars. *50th AIAA Aerospace Sciences Meeting including the New Horizons Forum and Aerospace Exposition*.

Sibille, L., Sadoway, D., Tripathy, P., Standish, E., Sirk, A., Melendez, O., and Stefanescu, D. (2010). Performance testing of molten regolith electrolysis with transfer of molten material for the production of oxygen and metals on the moon. *AIAA: 3rd Symposium on Space Resource Utilization*.

Sibille, L., Sadoway, D. R., Sirk, A., Tripathy, P., Melendez, O., Standish, E., Dominguez, J. A., Stefanescu, D. M., Curreri, P. A., and Poizeau, S. (2009). Recent advances in scale-up development of molten regolith electrolysis for oxygen production in support of a lunar base. In *Proc., 47th AIAA Aerospace Sciences Meeting, American Institute of Aeronautics and Astronautics (AIAA), Reston, VA*.

Simon, M. C. (1985). A parametric analysis of lunar oxygen production. In *Lunar Bases and Space Activities of the 21st Century*, volume 1, page 531.

Sirk, A. H., Sadoway, D. R., and Sibille, L. (2010). Direct electrolysis of molten lunar regolith for the production of oxygen and metals on the moon. *ECS Transactions*, 28(6):367–373.

Standish, E. (2010). *Design of a molten materials handling device for support of molten regolith electrolysis*. PhD thesis, The Ohio State University.

Teeple, B. S. (1994). *Feasibility of producing lunar liquid oxygen*. PhD thesis, Massachusetts Institute of Technology.

Turner, M. J. (2008). *Rocket and spacecraft propulsion: principles, practice and new developments*. Springer Science & Business Media.

Vai, A., Yurko, J., Wang, D., and Sadoway, D. (2010). Molten oxide electrolysis for lunar oxygen generation using in situ resources.

Wang, D., Gmitter, A. J., and Sadoway, D. R. (2011). Production of oxygen gas and liquid metal by electrochemical decomposition of molten iron oxide. *Journal of the Electrochemical Society*, 158(6):E51–E54.